A device for reducing the resistance of transom stern hulls

Ocean Engineering 235 (2021) 109351

Contents lists available at ScienceDirect

Ocean Engineering

journal homepage: www.elsevier.com/locate/oceaneng

A device for reducing the resistance of transom stern hulls

Arash Eslamdoost [a,*], Lars Larsson [a], Matz Brown [b]

[a] Department of Mechanics and Maritime Sciences, Chalmers University of Technology, Gothenburg, Sweden
[b] SSPA Sweden AB, Gothenburg, Sweden

ARTICLE INFO

Keywords:
Transom flow
Transom clearance
Recirculation zone
Resistance reduction
High-speed

ABSTRACT

A novel idea to reduce the resistance of a transom stern hull in displacement and semi-planing modes is investigated. By placing a spoon-shaped device in the recirculating zone behind the transom, the momentum of the forward-moving water will be absorbed, and a pushing force generated on the device. Numerical and experimental techniques are applied on a transom stern hull to optimize the shape and position of the device and to explore in detail the physics behind the gain. For the towed hull at a Froude number of 0.4, the maximum measured resistance reduction is 11%, while the computed maximum reduction is 17%. In self-propulsion with one propeller, the measured power reduction is 15%. The power cannot be computed with the applied propeller model, which is an axial body-force distribution in the propeller disk, but the reduction in thrust using the device is 11%. More significant gains are possible at smaller Froude numbers, while the effect is reduced at higher Froude numbers. Larger gains are achieved by splitting the thrust on two propellers.

1. Introduction

For boats and ships running at speeds in the semi-planing and planing speed ranges, transom sterns are the only viable option. Cruiser-type sterns cannot be used since the hull lines would then be strongly curved on the aft body, creating a large suction force, increasing both resistance and trim by the stern. The optimum transom size increases as the boat design speed increases (Larsson and Raven, 2010).

A model of a planing transom stern hull operating at two different speeds is shown in Fig. 1. In the lower speed range, the transom is wet, but there is a critical speed for transom stern hulls where the water surface leaves the transom tangent to the bottom, and after that, the transom becomes dry. Before this critical speed, the water is dragged along with the hull in a massively separated zone behind the transom. This is an unwanted flow feature and is considered a source of loss, increasing the hull resistance (Eslamdoost et al., 2015).

Merciar and Savitsky (1973) were among the first to propose a drag prediction algorithm for speeds in the pre-planing regime where the transom was still wet. The transom clearance phenomenon was studied by Oving (1986), who provided an empirical formula for the critical transom clearance Froude number as a linear function of the hull breadth to transom draft ratio.

Maki et al. (2006) conducted experiments with a series of geosim models of a destroyer. They provided a correlation between the static transom draft Froude number and the free-surface elevation behind the transom. They also developed a regression formula for estimation of the transom clearance as a function of the beam-to-draft ratio, transom-draft Froude number, and Reynolds number. A minor effect of free sinkage and trim on the critical Froude number was observed in comparison to a fixed model. They highlighted the importance of the wavefield on the transom clearance, which occurred earlier when the wave trough was located in the vicinity of the transom.

Based on measurements carried out on a series of simplified hull models with rectangular cross-sections, Doctors et al. (2007) provided a model for the transom hydrostatic drag to improve the traditional thin-ship formulation for resistance prediction. The transom flow measured for different cases showed that the water level drop at the transom was not linearly correlated with the ship speed but had a wavy trend. In contrast with an earlier study carried out by Doctors (2006), they detected a minor influence of the transom-draft Reynolds number on the transom clearance. These contradictory conclusions were related to the different measurement techniques used to detect the wave elevation at the transom.

For his doctoral thesis, Maki (2006) carried out a numerical and experimental analysis of the transom stern flow. A comprehensive literature review on transom flow research can be found in the thesis. Different flow regimes with varying characteristics of the free-surface behind the hull and the causes of the free-surface instability are

* Corresponding author.
E-mail address: arash.eslamdoost@chalmers.se (A. Eslamdoost).

https://doi.org/10.1016/j.oceaneng.2021.109351
Received 30 December 2020; Received in revised form 8 June 2021; Accepted 16 June 2021
Available online 2 July 2021

presented. Transom ventilation was also investigated.

The viscous and potential flow of a two-dimensional transom stern at increasing transom immersion was studied by Starke et al. (2007), who employed a free-surface fitting Reynolds-Averaged Navier -Stokes (RANS) method. Through comparison of potential flow and RANS results, they demonstrated that the critical Froude number decreases when viscous effects were neglected. They also concluded that the transom clearance occurred earlier at full scale compared to model scale resulting in a more significant transom resistance coefficient at full scale.

The same method and solver were employed by van der Ploeg and Starke (2013) to investigate the transom flow regimes for different three-dimensional (3D) transom geometries in model scale and full scale. They concluded that the scale effects influence the free-surface pattern mainly behind the transom. Moreover, they concluded that the wavelength is longer at full scale, and waves are less steep in this region.

Wyatt et al. (2008) carried out full-scale experimental measurements and numerical predictions of the wave pattern behind a semi-plaining transom-sterned vessel. The mean height and spectra of the breaking stern-waves were measured in-situ by a Light Detection and Ranging (LiDAR) sensor over a range of ship speeds both below and above the transom clearance Froude number. Two different viscous flow solvers were employed, and both displayed an over-suppression of the transom waves in the late wake after the initial onset of breaking. It was speculated that this resulted from an un-modelled turbulent process due to unsteady interaction of the propulsors and appendages, which may set up large organized turbulent structures that affect the dissipation of surface waves.

A detached eddy turbulence model was used by Bhushan et al. (2012) to investigate the vortical structures and associated instabilities of transom flow of the same full-scale vessel as tested by Wyatt et al. (2008). The transom wave elevation instability was attributed to the Karman-like transom vortex shedding, as both show the same dominant frequency. The authors showed that the transom vortex shedding influenced the dynamic sinkage and trim as well. They concluded that the instabilities in the flow did not show significant variation with scale, propeller, or motions.

Employing a RANS solver, Eslamdoost et al. (2015) investigated the physics of transom clearance of a planing hull. They reported an abrupt increase of the hull resistance at the critical Froude number where the transom is just fully ventilated. The peak in the resistance curve was caused by a sudden local increase in transom submergence related to the existence of a minimum in pressure coefficient and a maximum in streamline curvature at the transom edge.

Haase et al. (2016) investigated a catamaran hull at both model and full scale using an unsteady RANS approach and validated them against the model test. They reported the existence of a squashed horseshoe structure of the flow inside the stagnant area behind the transom, which showed an unsteady behaviour at higher transom Froude numbers. The transom drag was identified as a significant component of the total resistance (up to 70% at full scale), indicating the importance of accurate prediction of the transom flow.

Being interested in air-entrainment physics, Hendrickson et al. (2019) carried out an implicit Large eddy simulation of the turbulent transom flow beyond the critical transom clearance Froude number. The authors concluded that the convergent-corner-wave region formed immediately after the wake is ballistic, and thus only governed by the speed and geometry of the ship. Employing a Lagrangian cavity identification technique, they showed that the most potent air entrainment occurs at the position of wave breaking.

As presented above, several studies have been carried out to understand the transom stern flow physics from different perspectives. In the study described in this paper, we investigated a new technique to reduce ships' fuel consumption around transom clearance speed. The basic idea was to use the recirculating water energy and the breaking rooster tail wave behind the hull at speeds below the critical one, where the water clears the transom. A device was placed inside the recirculating water region to stop the water from moving forward (in the direction of hull movement). The goal was to reduce the energy loss in the recirculating water region. The device absorbs the momentum of the forward flowing water and pushes the hull forward. The overall result is a reduced total resistance. This idea has been patented in Sweden (Eslamdoost et al. (2020)) and has an international patent pending. The patent authorities know of no similar technique.

Fig. 2 shows a configuration used in the Computational Fluid Dynamics (CFD) simulations and experiments. Inserting the Transom Pushing Device (TPD) in the dead-water region splits the bare hull recirculating zone into two separate regions (Fig. 3). The shape and the horizontal and vertical positions of the device influence the flow and

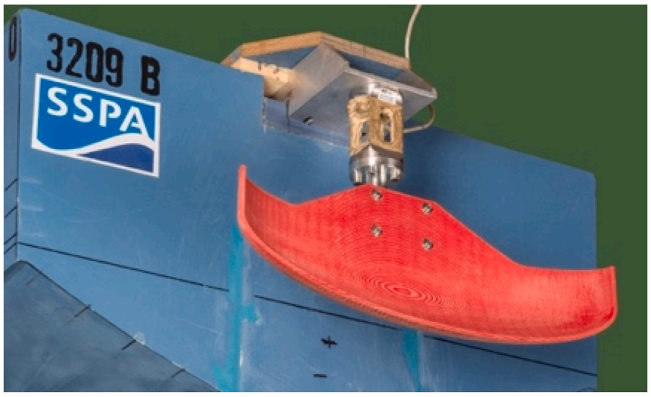

Fig. 2. Placing of the Transom Pushing Device (TPD) in the experiments.

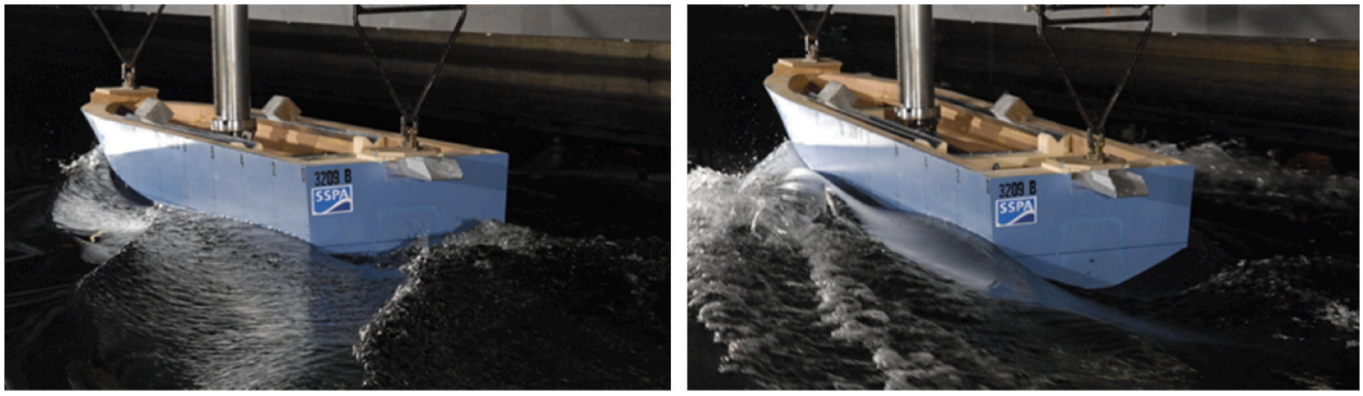

Fig. 1. The flow pattern around a planing transom stern hull at two different speeds. The hull transom is wet below the critical speed (left), and it becomes dry above the critical speed (right).

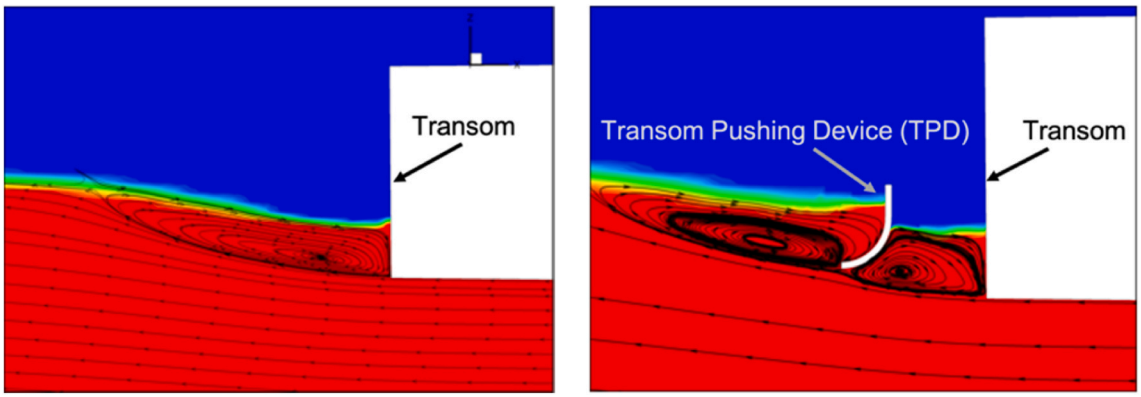

Fig. 3. Recirculating water region on the symmetry plane behind the bare hull transom (left) and with the TPD (right) at Froude number 0.4 and transom-draft Froude number of 1.7.

thus the forward pushing force.

The objective of the work was to understand the physics of the TPD better and to optimize the position both in towing and self-propulsion mode. The investigation was carried out using both CFD and experiments (referred to as Experimental Fluid Dynamics (EFD)).

In the following text, first, the example hull and the TPD are introduced. After that, the EFD technique is described, followed by a description of the CFD technique. Then the computed and measured results are presented, and finally, some conclusions are drawn.

2. Test case

The hull used in this study was a planing hull designed by SSPA (referred to as the SSPA hull in the following text). A body plan is presented in Fig. 4, and the longitudinal positions of the hull sections are shown in Fig. 5. The aft and fore perpendiculars are indicated by the numbers 0 and 20, respectively. Draft measurements were carried out at these sections. The towing point of the hull was 95 mm below the deck level and was located at section 6, shown in Fig. 5. In Table 1, the particulars of the hull are given.

The 3D printed propeller geometry is shown in Fig. 6. It has five blades with an outer diameter of 100 mm. This propeller is not designed to operate at low speeds, and thus its efficiency in the measurement speed range is lower than its best efficiency. It should also be mentioned that the ITTC guidelines for ship model testing state that the propeller diameter should be larger than 150 mm (ITTC 28 Resistance Committee, 2017). However, in the towing tank test carried out in this study, the selection of the propeller diameter used in the towing tank tests was constrained by the available hull size. Thus, the criterion recommended in the ITTC guidelines for propeller diameter in the model test was not fulfilled. Moreover, the 3D printed propeller was made of plastic that possibly deforms under high loading conditions. The blade deformation may result in performance degradation. These specifications can result in increased uncertainty of propeller performance measurement. To reduce the uncertainties incorporated with the propeller power measurement, only the relative change of propeller power with and without the TPD has been analysed in the paper.

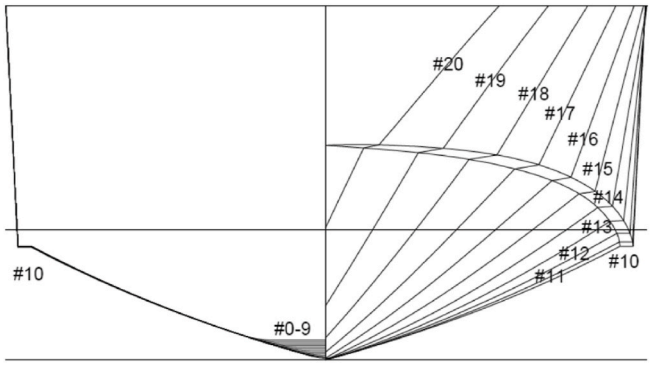

Fig. 4. The body plan of test the hull.

The location of the propeller and the TPD relative to the hull are shown in Fig. 7. Systematic variations of the TPD are reported in Sections 5.3 and 5.4. In CFD, the propeller is represented as a body force disk, shown in the figure. Note that this disk is vertical! This is to enable a better alignment with the grid to reduce numerical errors. However, even if the disk is upright, the body forces are directed along the imagined shaft, inclined 10° relative to the bottom. Note that no shaft was included in the computations. There was a physical shaft in the experiments, and the propeller was naturally at right angles to the shaft. The centre of both propellers was the same, and the position is shown in the figure.

A detail of the TPD mount is shown in Fig. 8. The TPD (1) is attached to a vertical bar (2), along which it can slide to different vertical positions. The bar is attached to a balance (3), which in turn is connected to a horizontal U-beam (4). This beam can slide longitudinally to position the TPD at different distances from the transom. The balance measures horizontal and vertical forces.

3. Experimental technique

3.1. Test facility

The tests were performed in SSPA's towing tank, which is 260 m long. The breadth and depth of the towing tank are 10 m and 5 m, respectively. The towing tank is spanned by a gantry carriage from which the ship model is towed. All tests were performed in calm water.

3.2. Test arrangement

The model was ballasted to the design loading condition. The draught was verified at the forward perpendicular (FP), midships (MS), and aft perpendicular (AP) on both sides of the model. During testing, the model was fixed axially to the carriage with a rod and an electrical transducer that measured the towing force exerted on the model. As the rod was adjusted to be parallel to the baseline, the force was measured in the horizontal direction at all tests. The model was kept on course by two guiding devices, one at each perpendicular. These devices also prevented the model from swaying and yawing while leaving it free to heave, roll and pitch.

When moving the TPD longitudinally, the centre of gravity moved backward. This was compensated by moving a ballast weight in the longitudinal direction.

The following signals were measured and registered by a computer

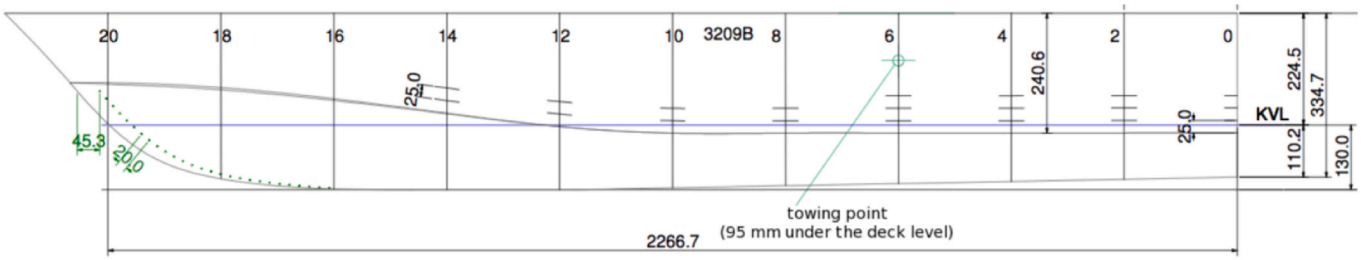

Fig. 5. The contour of the test hull. All lengths are given in millimeters.

Table 1
Hull particulars.

Length L_{PP} [m]	2.267	Beam B [m]	0.620
Length L_{WL} [m]	2.264	Displacement weight ∇ [N]	828.3
Forward draft σ_F [m]	0.131	Aft draft σ_A [m]	0.131

Note that this hull (transom size) was designed for Froude numbers around 1.0, while the main interest in the investigation described in this paper was in the Froude number range 0.2–0.5, where the transom is still wet. This means that the transom was larger than for a ship designed for this range. Quite often, fast planing hulls run at a lower speed rather than the design speed (naval craft, passenger ferries in the archipelago, fishing vessels, …). Thus, the present Froude number range is considered relevant.

Fig. 6. The propeller geometry (pressure side).

on the carriage:

- Model speed
- Towing force
- Vertical motion at FP
- Vertical motion at AP
- Vertical force on the TPD
- Horizontal force on the TPD
- Propeller shaft torque
- Propeller RPM

4. Numerical method

4.1. Numerical details

The numerical simulations were carried out with the code STAR-CCM+ 15.02. A Finite Volume method in combination with control volumes dominated by trimmed hex mesh was used in this code to solve the unsteady mass and momentum conservation equations in integral form. An implicit unsteady time-stepping method was used. This method has a wide stability range (Courant number larger than 1) and allows sizeable local time steps. The Volume of Fluid (VOF) method was used to obtain the volume fraction of the liquid, which added one more equation to the system of equations. Convective terms in this equation were discretized using the HRIC scheme. The free-surface interface was expected to be sharp since this equation resolves the free-surface within typically one cell. The k-ω SST turbulence model was used to compute the turbulence effects on the mean flow. The boundary layers were resolved down to the wall, and no wall functions were used. This system of equations was solved using a segregated iterative solution method based on the SIMPLE algorithm.

The simulations were carried out employing a Dynamic Fluid Body Interaction (DFBI) model to capture the dynamic sinkage and trim. Before starting the two degrees of freedom (free sinkage and trim) modelling, the simulations were carried out with the fixed sinkage and trim until the pressure, and viscous forces exerted on the hull were stabilized. Then the hull was released to sink and trim, and the DFBI solver started to update the equilibrium position of the hull iteratively.

In the case of the bare hull, a towing force was applied to the hull at the position where the hull was towed in the towing tank. The location of the tow force is shown in Fig. 5. To the extent possible, the tow force was kept parallel to the keel line during the resistance tests. In the computations, the magnitude of the tow force at each iteration is set equal to the hull's resistance computed from the previous iteration. The propeller was modelled employing a uniform distribution of an axial body-force inside a circular disk that encloses the propeller. Then the propeller thrust was included in the DFBI model as an external force acting on the hull (inclined 10°).

4.2. Grid

Only half of the geometry was used because the flow was considered symmetrical. Trimmed hexahedral grids and prism layers along walls were used to create the grids. Trimmed grids allow anisotropic local refinement around the hull and the free-surface. Four levels of refinement inside arbitrarily defined volumes were used for the free-surface and around the hull to capture the free-surface. The computational domain size and the overall grid distribution in the domain are shown in Fig. 9. As this study aimed to investigate the transom flow, the highest refinement level was used in this region, as shown in Fig. 10. The prism layer grid used to resolve the boundary layer is seen below the hull in the symmetry plane. Since no wall functions were used, y+ was set to be around 1 with an expansion ratio of 1.1 in the wall-normal direction.

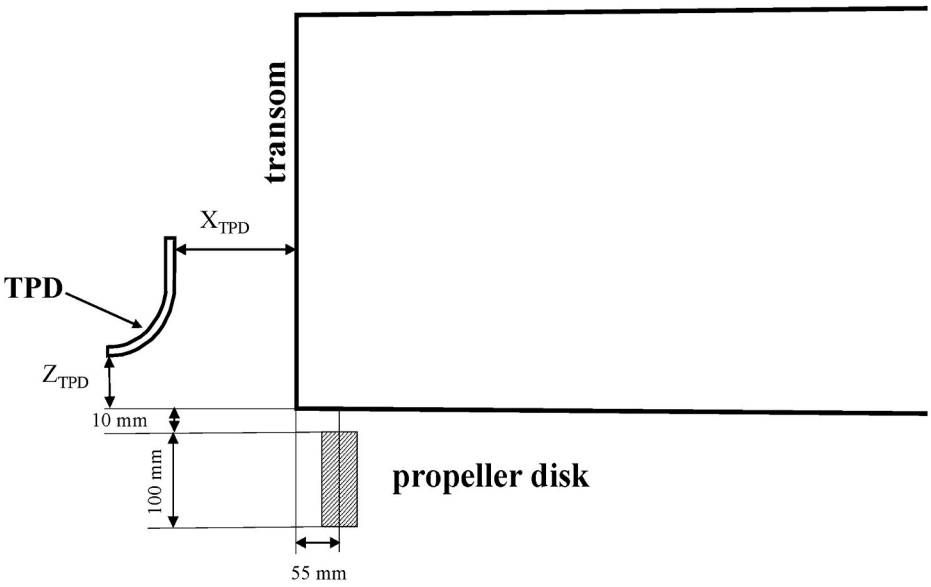

Fig. 7. Hull with TPD and propeller. The definition of the TPD position is also shown as X_{PD} and Z_{PD}. The coordinate system has its origin at the transom stern edge; X is directed forwards and Z vertically upwards.

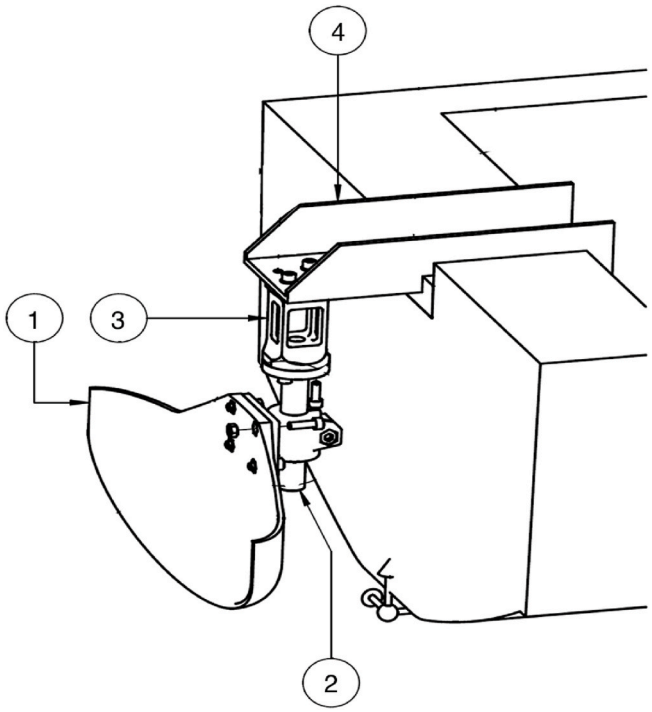

Fig. 8. Details of the TPD mount.

4.3. Verification

A systematic grid refinement study was carried out for Froude number 0.4 with the TPD at $(X_{TPD}, Z_{TPD}) \times \frac{100}{Lpp} = (5, 2)$ to obtain a suitable cell size, and the corresponding discretization uncertainty. The coordinate system is shown in Fig. 7. The study's Froude number was just below the critical Froude number, where the water clears the transom (Eslamdoost et al., 2015). Eight grids with systematically varied grid parameters were used. The number of cells in the coarsest grid was 0.944×10^6 and in the finest was 14.9×10^6. The convergence of the solution for the total resistance, R_T, non-dimensionalized by the displacement weight of the hull is shown in Fig. 11,. Since the grid is unstructured, the step size r_i on the horizontal axis is obtained as the third root of the total number of cells for the finest grid divided by the total number of cells for grid i. The finest grid is represented by $r = 1$ in this figure.

A formal verification based on the Least Squares Root method by Eça and Hoekstra was also carried out (Eça and Hoekstra, 2014). This showed that a good compromise between numerical accuracy and computational effort was obtained with the second finest grid, which was selected for further computations. The number of cells for this grid was 5.8×10^6, and the numerical uncertainty 4.04%. It should be noted that the verification method is for steady flows, while some unsteadiness was detected in the computations described here, particularly at Froude numbers below the critical one. A dependence on the time step may thus be expected.

4.4. Validation

Validation was done for the bare hull (BH) without the TPD. Fig. 12 shows the predicted and measured resistance against the Froude number as well as the magnitude of the comparison error in percent. At the most interesting Froude number, 0.4, the comparison error is around 4%, while the maximum error, 8%, occurs in the Froude number range 0.35–0.60. For the lowest Froude number, the comparison error is relatively large (around 14%). Note that the comparison error includes both computational and measurement errors. Unfortunately, no estimate of the experimental error was available, so a formal validation cannot be made. However, we can note that the comparison error for Froude number 0.4 is about the same as the numerical uncertainty, while it is more significant for the other Froude numbers. Aft draft and fore draft results are shown in Fig. 13. The correspondence between CFD and EFD is reasonably good except at the highest Froude number.

A systematic variation of the position of the TPD was carried out to obtain its optimum position. Fig. 14 shows the variation of the time-averaged measured and computed horizontal force acting on the TPD both on the bare hull and the self-propelled hull at Fn = 0.4. The non-dimensional force acting on the TPD in the interval studied varies within ±15% of the non-dimensionalized total resistance at this speed. The horizontal force acting on the TPD points forward when the TPD is positioned close to the transom and decreases as the TPD is positioned further from the transom. The force even changes direction when the TPD is positioned sufficiently far from the transom. The trends of the

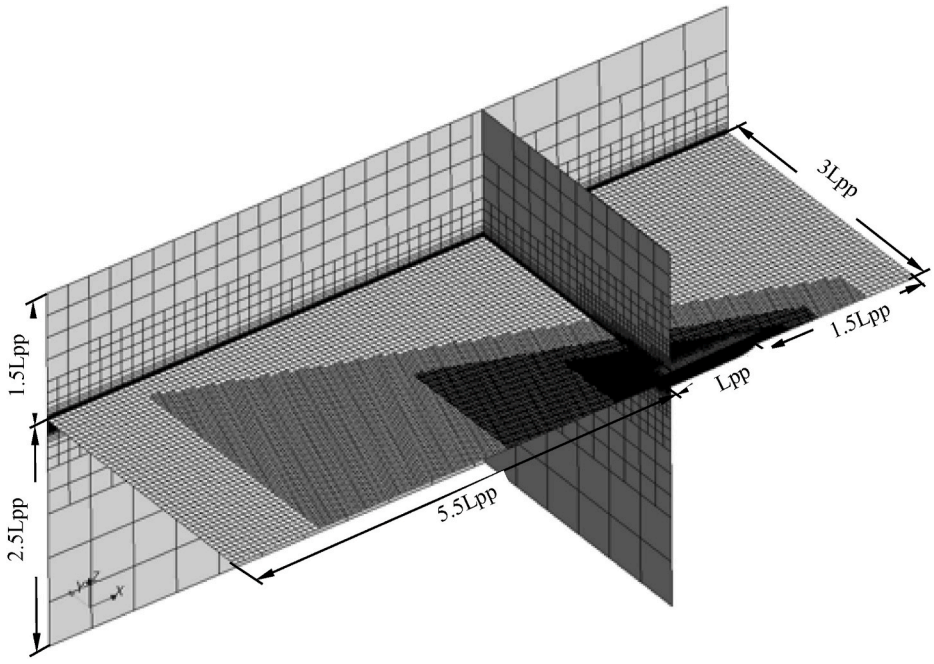

Fig. 9. The structure of the mesh illustrating the refined zones. Arrows show the dimensions of the computational domain expressed in the hull Lpp.

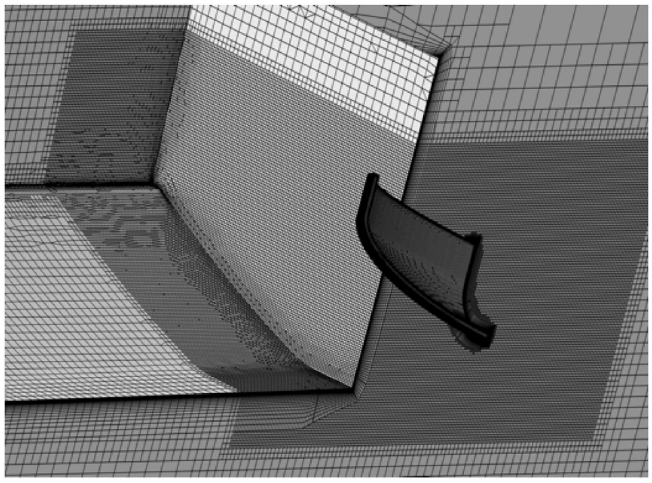

Fig. 10. Closer look at the mesh around the transom and TPD (bow to the left).

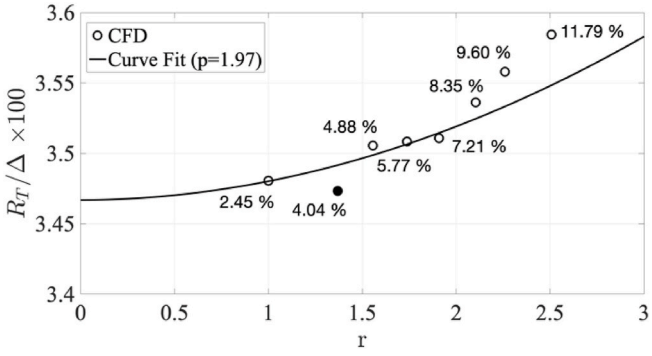

Fig. 11. Convergence of the total resistance coefficient with grid refinement at $Fn = 0.4$. The full circle indicates the grid used in this study. The grid refinment ratio is denoted by r. The percentage of the numerical uncertainty of the computed resistance for each grid is shown next to the data points.

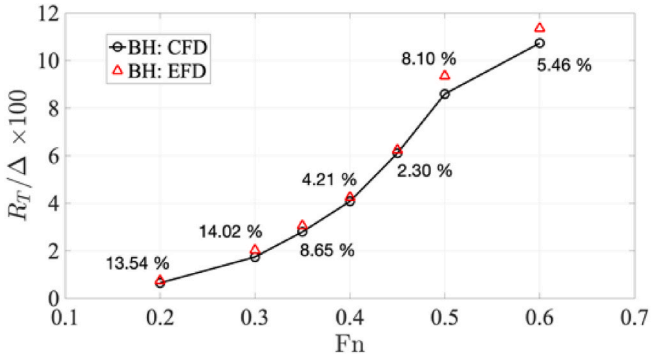

Fig. 12. Measured (EFD) and computed (CFD) total resistance for the bare hull.

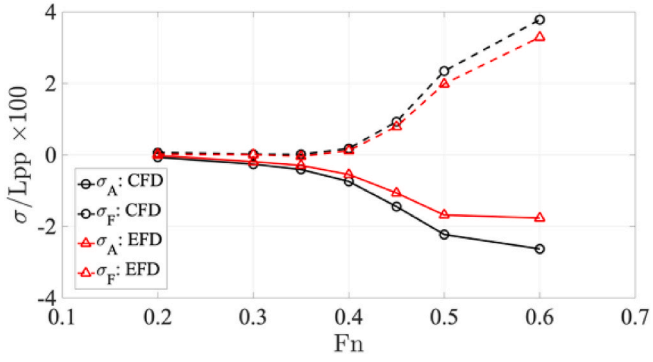

Fig. 13. Measured (EFD) and computed (CFD) aft draft, σ_A, and fore draft σ_F, for the bare hull.

measured and computed force variations agree well with each other; however, the agreement level is much better when the TPD is located close to the transom ($X_{TPD}/Lpp \times 100 < 6$). We should keep in mind that the TPD is placed in the core of a turbulent flow region which may show large instabilities. Thus, considering the complicated flow physics, the agreement between the measured and computed horizontal TPD force is

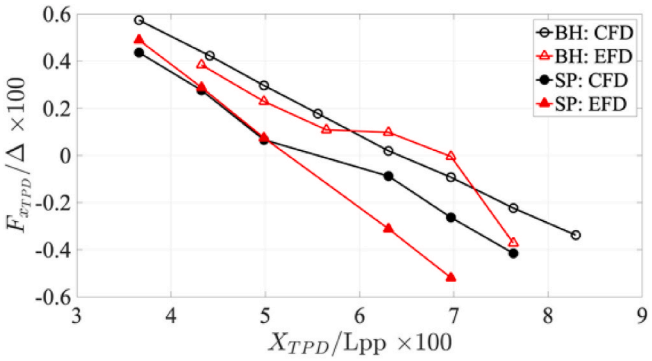

Fig. 14. Measured (EFD) and computed (CFD) horizontal force acting on the TPD on the bare hull (BH) and the self-propelled hull (SP) at Froude number 0.4 ($Z_{TPD}/Lpp \times 100 = 0.84$).

deemed satisfactory. It should be noted that a large pushing force does not necessarily mean a large resistance reduction. The TPD interacts with the transom flow and thus alters the transom resistance. Therefore, to evaluate the performance of the TPD, we should consider the total resistance of the hull, including the TPD, and not only the force acting on the TPD. The physics of the TPD resistance reduction mechanism is discussed in 5.2.

5. Results

5.1. Design of the TPD

The TPD utilizes the energy in the recirculating water behind the transom in the lower speed ranges when the transom is still wet. In the initial design phase, two different flat plate geometries were placed in the recirculating water region (Fig. 15). The plates were placed at the same longitudinal distance from the transom, and an optimization study was carried out to obtain the largest resistance reduction as a function of vertical distance from the transom edge. These preliminary studies showed a resistance reduction of 2.8% for the rectangular plate and 4.6% for the triangular plate at Froude number 0.4. The pressure distribution on both sides of the plates is shown in Fig. 16 and Fig. 17.

The high pressure on the front side of the rectangular plate shows that the corners penetrate the free-stream flow, which reduces the plate's efficiency. Thus, as a modification to the initial design, a triangular TPD was generated by trimming the lower corners of the rectangular plate. The reduced pressure on the same face of the triangular TPD shows that trimming the lower corners of the rectangular plate produces a favourable result, and the triangular TPD does not penetrate the free-stream flow any longer. As mentioned, this modification improved the performance of the TPD by about 2% in comparison to the rectangular TPD.

However, the flat triangular TPD is not streamlined, and its sharp edges may increase the system resistance in cases where it penetrates the free-stream flow. To minimize the risk of increased resistance, a curved surface that allows the free-stream flow to pass smoothly is better than a flat plate. Moreover, the TPD can cover a larger recirculating water area if its form is adapted to the structure of the recirculating region, which itself is a function of the transom shape as well as the operating speed of the hull. Fig. 18 shows the streamlines behind the transom in half of the recirculating region. There are also several cross-sections shown in this figure. The dark blue area shows the flow moving backward, and the red colour highlights the region where the flow moves in the forward direction. The TPD function is to take advantage of the energy in this flow region and reduce the resistance. The cross-sections marked with red can be used to design an improved TPD form adapted to this region. The projected area of the new design in Fig. 19 is taken from one of the cross-sections, and its edges are curved backward to avoid a sudden increase in resistance in cases where it moves out of the recirculating water zone. The new design of the TPD is shown in Fig. 20. The new design offered a resistance reduction of 5.7% in the preliminary design stages, which was 1.2% better than the triangular TPD. Note that this improvement was obtained in the early design phase of the project, and through a systematic variation of TPD position, we managed to improve the performance considerably. The systematic variation of the TPD position is presented in Section 5.3.

5.2. Physical understanding

The basic idea behind the TPD is to take advantage of the momentum in the forward direction found in the recirculating zone behind the transom. A device with significant resistance in this forward flowing water would create a pushing force when attached to the hull. However, preliminary calculations indicated that there might be other important unexpected effects. In this section, we describe how CFD was used to investigate the physics of the TPD.

5.2.1. Global versus local effect

The first question is whether the TPD effect is related to the local flow behind the transom or to the global flow. This was investigated by changing the hull attitude (sinkage and trim) to determine whether the TPD acts as a trim plane or alternatively reduces the resistance by reducing the size of the (too large) transom.

To investigate the effect of local and global flow changes, three cases

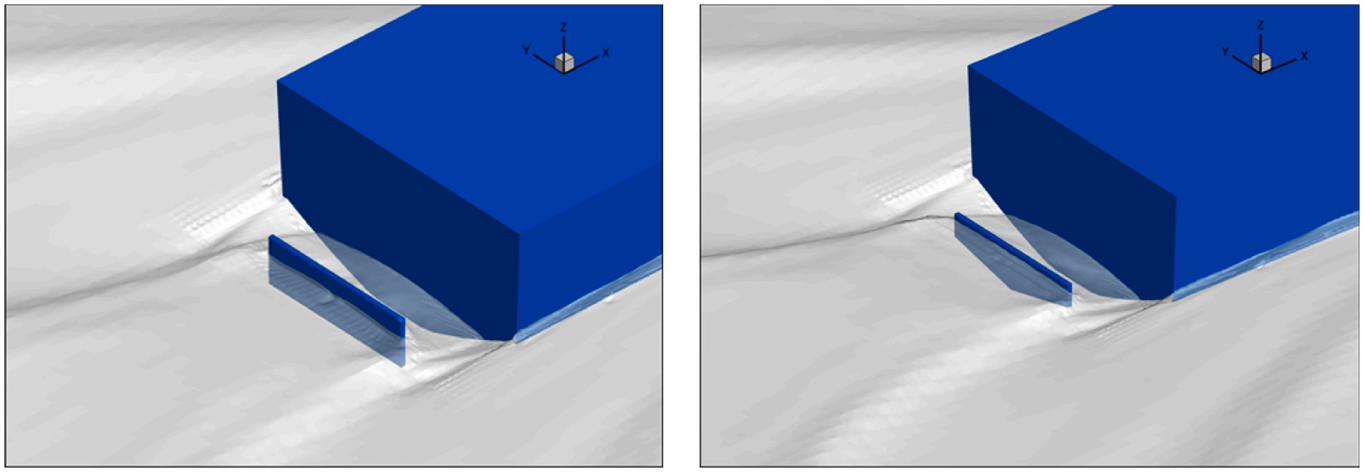

Fig. 15. Application of a rectangular plate (left) and a triangular plate (right) as a TPD.

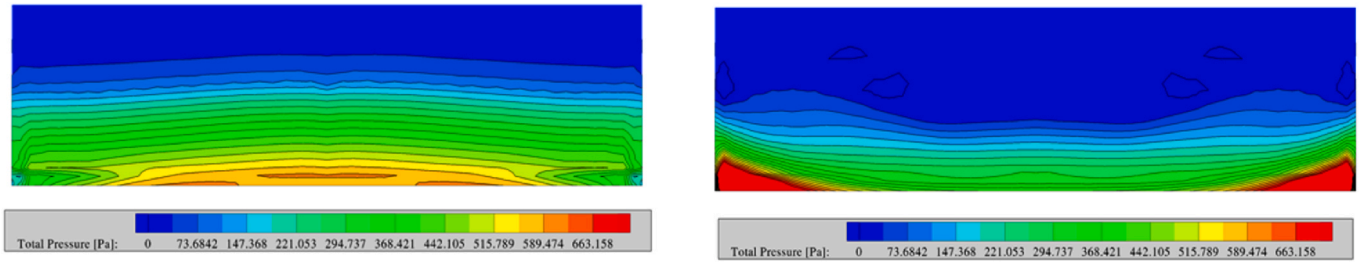

Fig. 16. Pressure distribution on the rectangular TPD, with the backward-facing surface shown on the left and the forward-facing surface on the right.

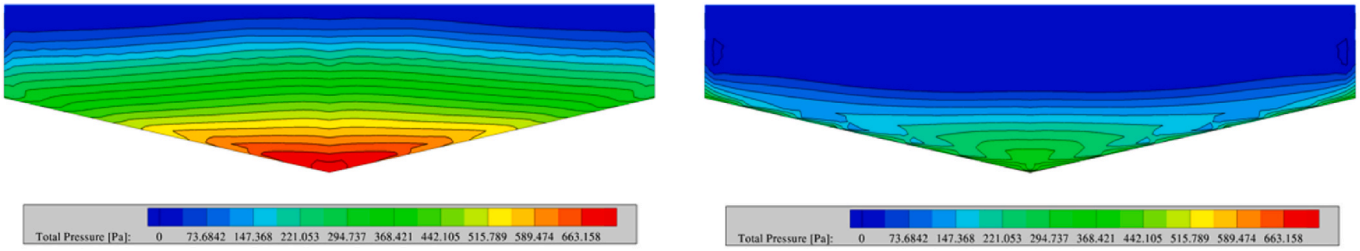

Fig. 17. Pressure distribution on the triangular TPD, with the backward-facing surface shown on the left and the forward-facing surface on the right.

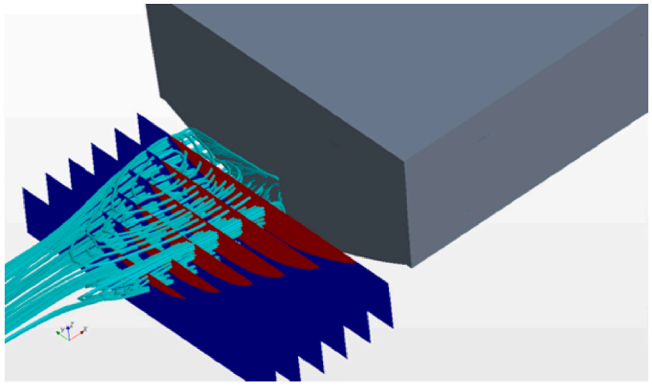

Fig. 18. Streamlines in the recirculating water region and the split of the flow based on its direction. The flow moving backwards is shown in dark blue, and the flow moving forwards is shown in red. (For interpretation of the references to colour in this figure legend, the reader is referred to the Web version of this article.)

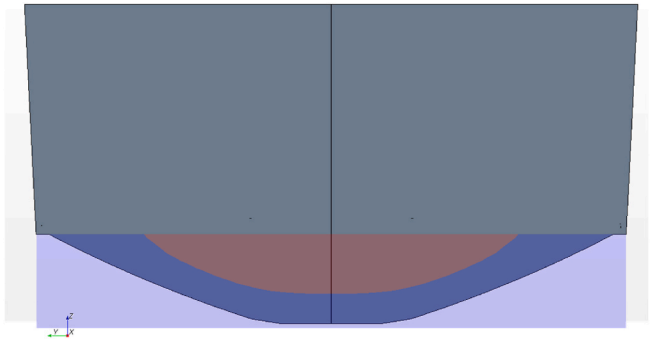

Fig. 19. One of the cross-sections from Fig. 18.

were compared for the optimum position (shown in Fig. 29) of the TPD at $X_{TPD}/Lpp \times 100 = 5$ and, $Z_{TPD}/Lpp \times 100 = 1.1$ at Fn $= 0.4$, without the propeller. In addition to the bare hull without the TPD (BH) and with the TPD (BHPD), a case was run with the same sinkage and trim as BHPD

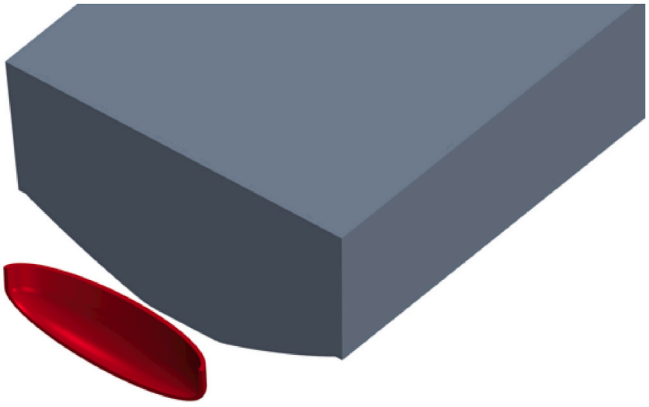

Fig. 20. Wake adapted TPD design.

but without the TPD (BH_BHPD). The effect of changes in sinkage and trim could then be evaluated. The non-dimensionalized fore and aft drafts of BH ($\sigma/Lpp \times 100$) were 0.18 and −0.74, respectively. The non-dimensionalized fore and aft draft of BHPD and thus BH_BHPD were 0.11 and −0.68, respectively. These drafts resulted in a trim angle of 0.5° for BH and 0.4° for BHPD, and thus BH_BHPD. The results are shown in Table 2, where the resistance contributions are split into three components: the hull excluding the transom (hull), the transom, and the TPD.

The last row of Table 2 shows that the total resistance changes very

Table 2
Effect of sinkage and trim changes on the resistance component of bare hull without the TPD (BH), with the TPD (BHPD), and the bare without TPD that has the same sinkage and trim as BHPD (BH_BHPD). The resistance components are given in Newtons, and also in percentage of the displacement weight ($\frac{F_x}{\Delta} \times 100$) inside parentheses.

	BH	BH_BHPD	BHPD
Hull	42.6 (5.1)	41.5 (5.0)	41.8 (5.0)
Transom	−7.8 (−0.9)	−7.5 (−0.9)	−8.9 (−1.1)
TPD	–	–	−4.6 (−0.5)
Total	34.8 (4.2)	34.0 (4.1)	28.3 (3.4)

little due to the sinkage and trim change, from 34.8 N to 34.0 N. The effect of adding the TPD (for the same trim) is an order of magnitude larger, a change from 34.0 N to 28.3 N. The resistance reduction due to the changed sinkage and trim mainly comes from the hull (42.6 N changed to 41.5 N). In contrast, the transom contribution change is minor (−7.8 N to −7.5 N). Adding the TPD increases the transom contribution considerably more (from −7.5 to −8.9), while the most significant resistance reduction by far is due to the force from the TPD (−4.6 N). This investigation thus confirms the original idea that it is the force on the TPD that causes the resistance reduction *when the TPD is in its optimum position*.

One effect which was not foreseen in the original TPD idea was the increase of water level on the transom, which increases its pushing force. As we have seen in Table 2, there is indeed such an effect, at least for this condition. In Fig. 21, the relative importance of the TPD and the increase in transom pushing force is shown for varying *longitudinal* positions of the TPD but with the vertical position fixed to the optimum at $Z_{TPD}/Lpp \times 100 = 1.1$. There is also a curve for the change in hull resistance (excluding transom).

The TPD is the most significant contributor to the pushing force at all longitudinal positions. The transom change contribution is much smaller but positive. For large distances, the transom effect approaches the TPD effect. The hull effect is small and positive at small distances but negative when the TPD is distant from the transom.

The rise in water level at the transom when the TPD is in the optimum position is shown in Fig. 22. For this case, the increase in the wetted area on the transom is 9.6%.

It may be of interest to also look at the water levels on the two sides of the TPD. These are shown for the reference case in Fig. 23. The water level is much higher on the rear surface, as expected. This indicates the different pressures on the front and rear surfaces of the TPD that give the pushing force. The pressures are presented in Fig. 24. In Fig. 25, the pressure forces on the two sides are displayed as a function of the TPD position. The positive contributions to the pushing forces from the rear (concave) surface are much larger than the negative contributions from the front (convex) surface. This is particularly so for the optimum longitudinal position and at positions closer to the transom. At positions further from the transom the positive force is reduced, and the negative one is increased (absolute value), which means that the total TPD force is decreased considerably. Note that all this is for the optimum vertical position ($Z_{TPD}/Lpp \times 100 = 1.1$).

If the vertical position of the TPD is varied, the findings change. Fig. 26 shows the contributions from the TPD, the transom, and the hull (excluding the transom) when the axial position was fixed to the optimum ($X_{TPD}/Lpp \times 100 = 5$), while the vertical position was varied. Apparently, the relative contributions change drastically for non-optimum vertical positions. But, interestingly, the sum of the contributions, i.e., the total effect, is relatively constant. If the TPD is pushed down into the free stream water moving backward, its pushing force will naturally be reduced. When it approaches the level of the transom edge, the TPD will create a drag force. However, the high pressure in front of the TPD in this position will raise the water level on the transom, thereby increasing its pushing effect. Also, the TPD will act as a trim plane and create a bow-down trim, which reduces the hull drag due to the too large transom.

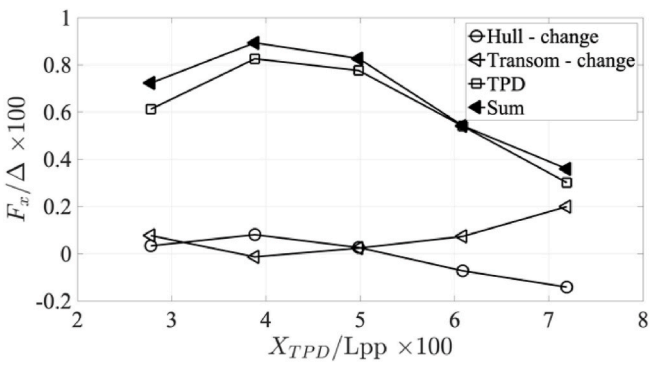

Fig. 21. Contribution of the pushing force from TPD, transom, and hull against TPD horizontal position variations.

When the TPD is lifted above the optimum position, the pushing force is naturally reduced. It does not take full advantage of the recirculating flow in this position. However, even in this case, there is a rise in the water level on the transom, which increases its pushing effect and partly compensates for the loss in TPD force.

5.2.2. TPD effect on the wave pattern

The basic idea is that the TPD will take advantage of the forward-moving water in the recirculating zone. The question is whether it also changes the transmitted wave height. Fig. 27 shows the wave pattern for the optimum position at Fn = 0.4. A reduction in wave height caused by the TPD is seen, at least close to the hull. Fig. 28 shows the wave height in the symmetry plane behind the hull. Again, a reduction in wave height is seen close to the hull, but the effect seems to decay with distance from the hull.

5.3. Systematic variations with and without a propeller

In the figures above, the optimum position of the TPD has been used as a reference, and the effect of variations has been discussed, referring to this section. Here, the entire matrix of variations will be presented. To obtain the optimum position of the TPD, computations with a systematic variation in position were carried out with and without the TPD for the towed hull and the self-propelled one. The gain is visualized in Fig. 29. The maximum gain, 16.75%, is at the reference position, $(X_{TPD}, Z_{TPD}) \times \frac{100}{Lpp} = (5, 1.1)$. As seen in this figure, the gain is relatively constant with X_{TPD} variation around the optimum height, but moving further away from the optimum height, the gain drops considerably.

The corresponding gain for the self-propelled case is presented in Fig. 30. It would have been more interesting to give the reduction in delivered power, but that cannot be computed using the current approach with a body-force disk representing the propeller.

The optimum occurs at the same axial position but at a smaller vertical distance from the transom edge, $(X_{TPD}, Z_{TPD}) \times \frac{100}{Lpp} = (5, 0.8)$. The magnitudes of the gains are smaller. The maximum gain in the self-propelled case is 11.9%. From Fig. 30, it also appears that the best efficiency region for the TPD is more confined relative to the results from the towed hull. This is attributed to the smaller recirculating region behind the transom in self-propulsion compared to the towed hull. The propeller accelerates the flow on the afterbody. Thus, the flow has higher momentum, which makes it less prone to break behind the transom. The result will be a more confined recirculating region which has less energy for the TPD to harness.

A comparison between computed and measured resistance reductions for the bare hull is shown in Fig. 31. The maximum gain estimated using CFD is about 17%, while the measured gain from the tests indicates approximately 11% resistance reduction. The CFD and EFD optimum positions are observed to be different. In this figure, we compare changes in forces, which are about one order of magnitude smaller than the total resistance. This may result in a significant comparison error. Direct comparison of the hull resistance (Fig. 12) or the horizontal TPD forces (Fig. 14) results in a much better agreement level, especially when the magnitude of the force is large.

In the self-propelled hull simulations, an axial body-force model has been used for modelling the propeller. Since the propulsive efficiency of the propeller is not known, we cannot compute the delivered power. Instead, we present the computed effective power (resistance × hull speed) and the measured delivered power (torque × rotation rate) below. Note that these quantities are not directly comparable. Fig. 32

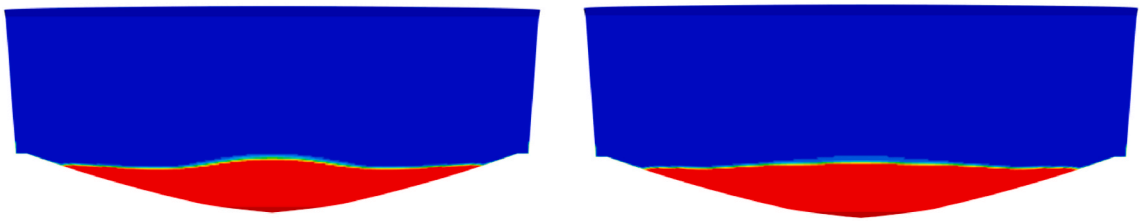

Fig. 22. The wetted surface on the transom without and with TPD at Froude number 0.4. The water is shown in red. (For interpretation of the references to colour in this figure legend, the reader is referred to the Web version of this article.)

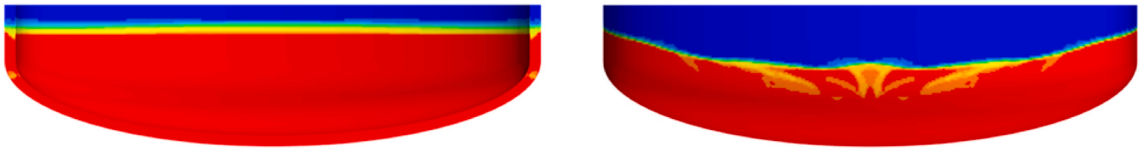

Fig. 23. Wetted surface on TPD at Froude number 0.4. Rear surface(left) and front surface (right).

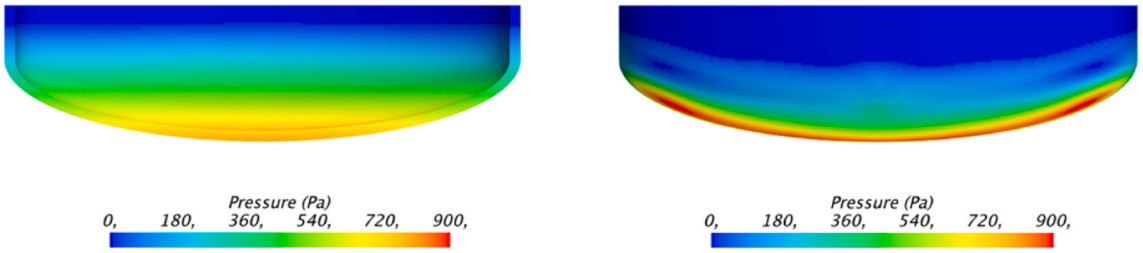

Fig. 24. Pressure distribution on the TPD at Froude number 0.4. Rear surface (left) and front surface (right).

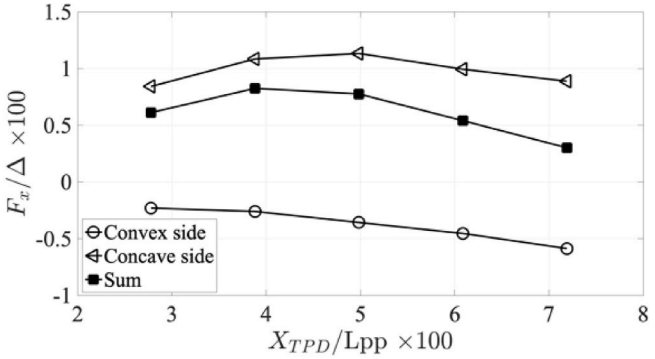

Fig. 25. Contribution to the total pushing force on the TPD from the two sides.

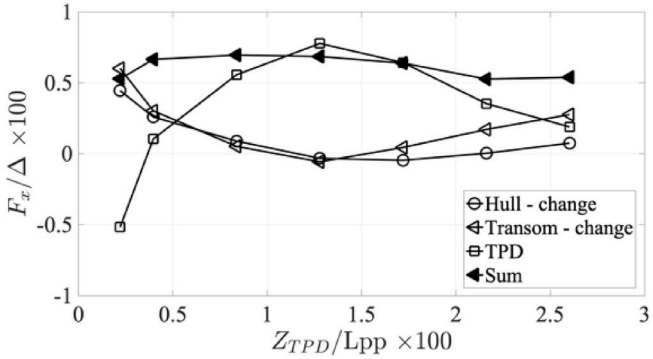

Fig. 26. Contribution of the pushing force from TPD, transom, and hull for TPD vertical position variations. The axial position is fixed to the optimum ($X_{TPD}/Lpp \times 100 = 5$).

shows the gains achieved by placing the TPD at different distances from the transom. The reference effective power is computed from the resistance of the simulated self-propelled hull, and the reference delivered power is obtained from the self-propulsion measurement at Fn = 0.4, both without the TPD. Interestingly, we can see that the gain in the measured delivered power in self-propulsion (Fig. 32) is more significant than the measured resistance reduction of the towed case (Fig. 31). This may sound to be in contrast with an earlier conclusion in this section that, due to a smaller recirculating water region in self-propulsion, the gains in resistance reduction will be smaller compared to the towed case. However, we should not forget the effect of the propulsive factors.

Presumably, the main contribution to the change in delivered power will come from the resistance change. We should also keep in mind that the transom stern hulls are mainly designed to operate at speeds beyond the transom clearance Froude number. Therefore, the propeller of a transom stern vessel, which operates at speeds below the transom clearance Froude number, operates in an off-design condition, where its efficiency is far from the best efficiency point. A reduction of the ship resistance by the TPD results in an unloading of the propeller, and thus a better efficiency is achieved. Therefore, the TPD benefit is achieved not only by the reduced resistance but also by the improved propeller efficiency. This is most likely the reason for the more significant measured total gain in self-propulsion (15.2%) compared to that of the towed case (11%).

The optimum position of the TPD at Fn = 0.4 was used to study the effect of the TPD on power reduction at other speeds as well. Fig. 33 shows the gain in self-propulsion versus Froude number at different speeds. Somewhat surprisingly, the gain increases when the Froude number is reduced. The most significant gain in power obtained from EFD is about 25% at Fn = 0.2. In the range Fn = 0.3 to 0.5, the gains

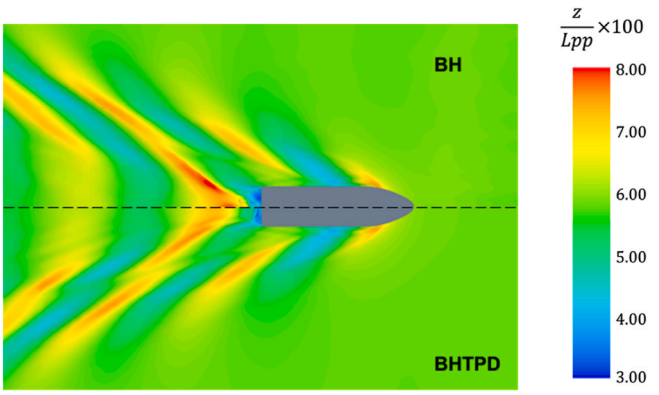

Fig. 27. Wave pattern at optimum TPD position at Froude number 0.4. Above: without TPD. Below: with TPD.

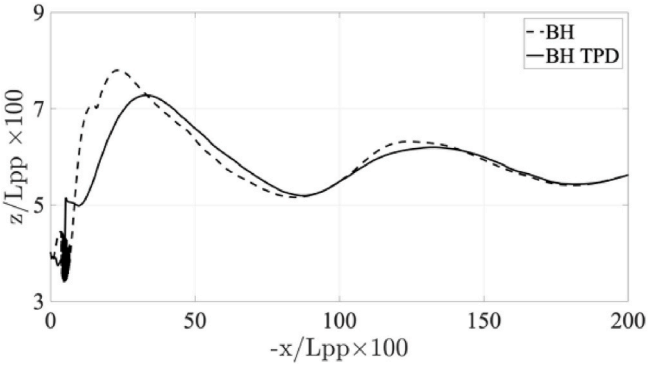

Fig. 28. Wave height in the symmetry plane behind the hull. BH: without TPD. BHPD: with TPD. Bow to the left.

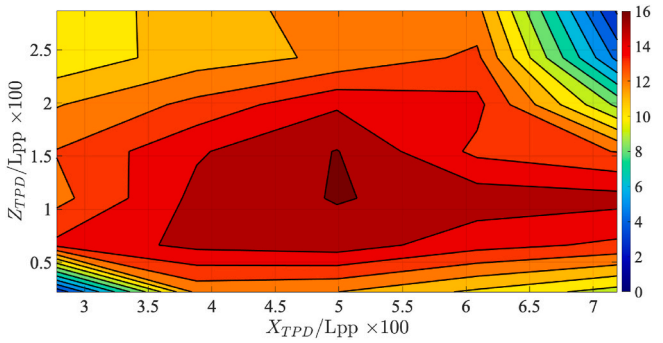

Fig. 29. Visualization of gains with TPD for different positions. Bare hull.

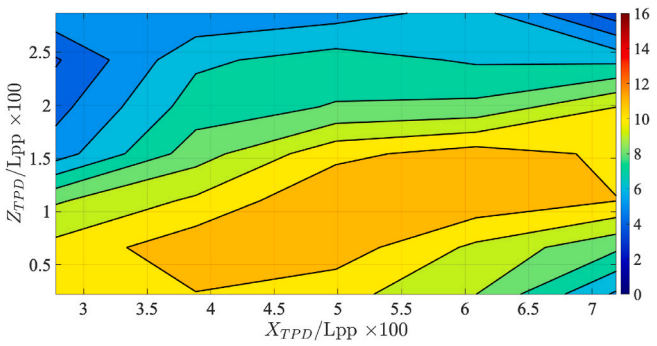

Fig. 30. Visualization of resistance reduction with TPD for varying positions. Self-propelled hull.

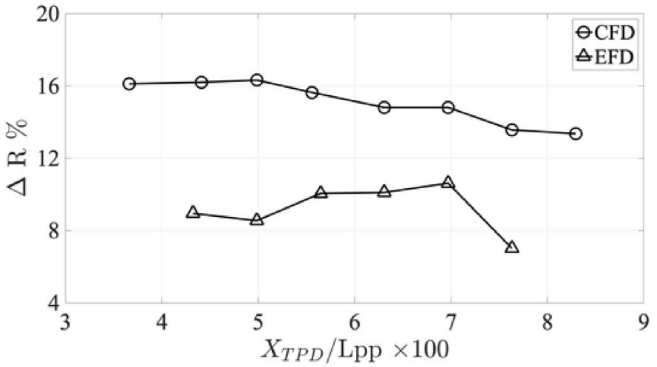

Fig. 31. Comparison between computed and measured resistance reductions (ΔR).

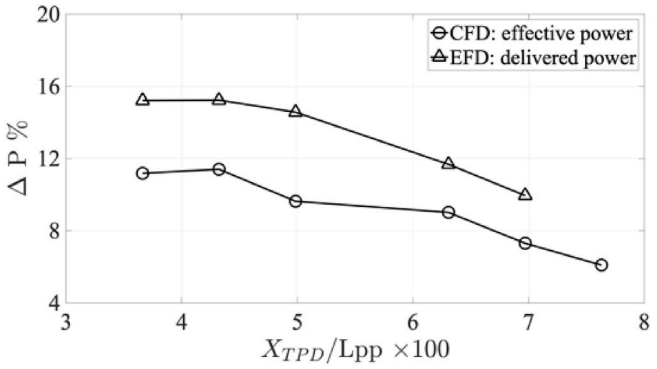

Fig. 32. Computed reduction in effective power compared with the measured reduction in delivered power (ΔP).

are between 13 and 18%, which is much more than anticipated. In the same range, the effective power gains computed from CFD simulations vary between 10 and 14%. So, in both cases the reductions are considerable.

The performance of the TPD at Froude numbers above the transom clearance Froude number is surprising. Fig. 34 displays the computed free-surface profile at the symmetry plane with and without the TPD at Froude number 0.5. The transom is fully ventilated at this Froude number; however, both the CFD and EFD data show that the TPD has reduced the power by about 14%. Inserting the TPD into the transom region at this Froude number alters the transom flow differently. As seen in Fig. 34, the interaction of the TPD and the transom waves results in an increase of transom clearance Froude number. The transom is not fully ventilated any longer, and consequently, the transom drag is reduced. The TPD contributes to the resistance reduction through a pushing force as well. Moreover, in contrast to the conclusion made in section 5.2.1 for the optimum TPD position at Froude number 0.4, the TPD does alter the hull attitude slightly at this Froude number. As seen in Fig. 34, in the presence of the TPD, the hull trim angle is somewhat reduced (reduced aft draft), which in turn reduces the hull resistance. Therefore, at this Froude number, the TPD reduces the total resistance by altering both the local and the global flow.

5.4. Two propellers

In this section, the performance of the TPD is reported for a two-propeller arrangement at Froude number 0.4 and compared with the one-propeller case presented above. As stated in the computational method description section, a body-force model has been employed to

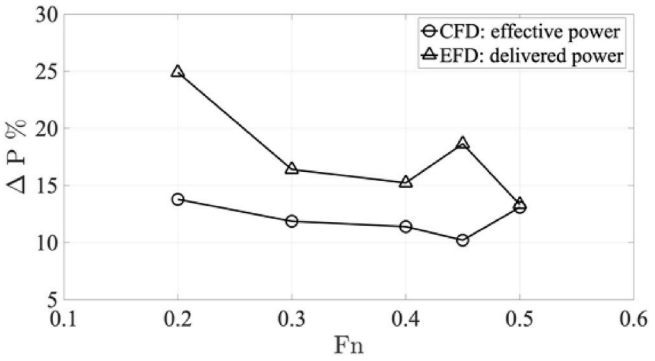

Fig. 33. Measured and computed gains against Froude number.

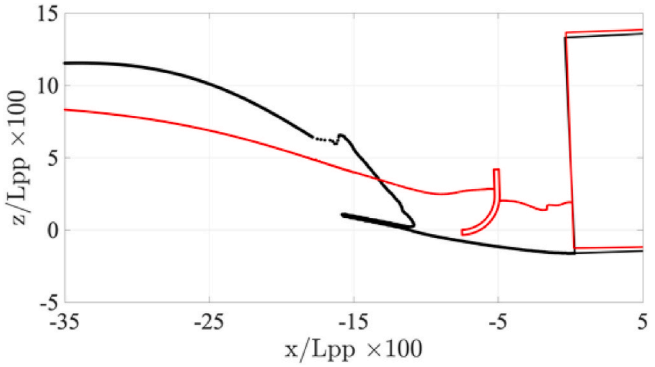

Fig. 34. Free-surface profiles at the symmetry plane with the TPD (red) and without the TPD (black) at Fn = 0.5. (For interpretation of the references to colour in this figure legend, the reader is referred to the Web version of this article.)

model the propeller effect. The dark blue areas in Fig. 35 show the regions where the body-force has been deployed to accelerate the flow. In the case of one propeller, the propeller centre is placed on the hull symmetry plane (diameter = 100 mm). In this section, two propellers of smaller diameters (diameter = 70 mm) are placed 150 mm away from the hull symmetry plane (Fig. 35).

Table 3 shows the results obtained from CFD self-propulsion simulations in the presence of one propeller and two propellers, with and without the TPD. The optimum TPD position obtained from self-propulsion systematic optimization is used for all these simulations. If we compare only the self-propelled hulls without the TPD, we notice that the hull resistance (propeller thrust) has increased by about 1.5 N when two propellers are used. Since the sinkage and trim angles for these hulls are almost the same, only the local flow changes contribute to

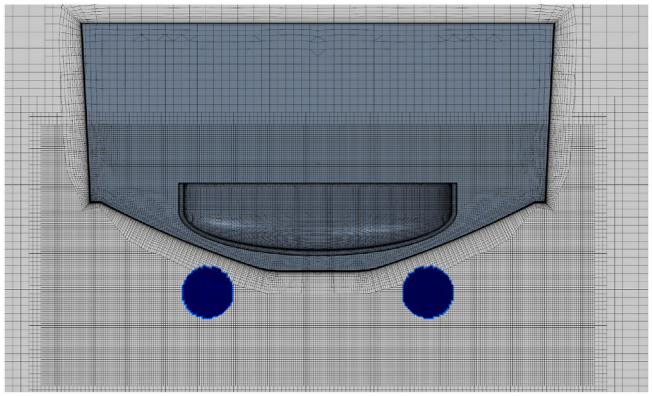

Fig. 35. Body-force application region for two propellers.

Table 3
Variation of hull aft draft, trim, and resistance for BH: bare hull, SP: self-propulsion with 1 and 2 propellers with and without the TPD. The numbers inside the parentheses are non-dimensionalized values. The non-dimensional aft draft and resistance are obtained from $\sigma_A/Lpp \times 100$ and $R_T/\Delta \times 100$, respectively.

	Aft draft [mm]	Trim [degrees]	Resistance [N]	Resistance reduction [%]
BH	−16.9 (−0.75)	0.49	34.0 (4.1)	–
SP: 1 Propeller	−19.3 (−0.88)	0.61	32.2 (3.9)	–
SP: 1 Propeller + TPD	−14.9 (−0.66)	0.39	28.4 (3.4)	11.9
SP: 2 Propellers	−19.6 (−0.86)	0.60	33.8 (4.1)	–
SP: 2 Propellers + TPD	−14.8 (−0.65)	0.39	28.9 (3.5)	14.4

the increased hull resistance. The leading cause is the decreased wetted area of the transom with two propellers compared to the self-propulsion simulation with one propeller. As a result, the transom drag for the hull with two propellers increases about 1.3 N, i.e., almost the entire drag difference between the cases.

Based on the numerical study of the TPD position optimization in self-propulsion, we know that the TPD reduces the self-propelled hull resistance (thrust) by 11.9%. The resistance reduction increases to 14.4% when two propellers are used. The sinkage and trim of these hulls are the same, and again the local flow changes must be responsible for the lower resistance of the hull with two propellers. In fact, the pushing force of the TPD is slightly smaller for the hull with two propellers (0.6 N in comparison to 1.2 N). However, due to the interaction between the TPD and the transom, the wetted surface area of the transom becomes the same for both hulls. Remember that the transom wetted surface area without the TPD was smaller for the hull with two propellers. In the presence of the TPD, the hulls have precisely the same wetted surface area and thus transom pushing force. Consequently, the gain is more significant for two propellers.

6. Conclusions

A Transom Pushing Device (TPD) has been developed to reduce the resistance of transom-stern planing hulls, which operate at off-design conditions, where the transom is not ventilated, and a recirculating water region exists behind the transom. A spoon-shaped TPD is considerably more efficient than a flat one. Rectangular and triangular plates were investigated, but both were inferior to the newly developed spoon shape.

The TPD resistance reduction is mainly achieved through modification of pressure distribution in the aft region. The waves behind the hull are also reduced by the TPD, but this effect diminishes in the far wake.

For the optimum position of the TPD, its main effect is, as expected, a pushing force generated by the device when it is located in the recirculating flow. There is also a positive effect of a water level rise at the transom, but that is much smaller. In the low-speed range, the impact on sinkage and trim is minor; however, the TPD can act as a trim plate at speeds just above the transom clearance Froude number.

For other positions of the TPD, particularly in the vertical direction, its role changes. For a too low placement (closer to the transom edge), the pushing force is reduced considerably and may become negative. However, this effect is compensated to some degree by increasing the water level on the transom and a smaller trim of the hull.

Systematic variations in position for the towed case showed a maximum resistance reduction in CFD by 17%, while the measured maximum gain in EFD was 11%. This is for the most interesting Froude number, Fn = 0.4.

For the self-propelled case, the maximum resistance (thrust)

reduction was 11% in CFD, while the reduction in power for EFD was 15%, again at Fn = 0.4. The propeller jet stream sweeps the transom wave further downstream, making it less prone to break and fill in the transom hollow. As a result, the recirculating region behind the transom becomes smaller than that of the towed hull, and consequently, the gain in resistance is reduced. However, the total gain in self-propulsion is not achieved solely by the resistance reduction. The propeller of a planing hull at speeds below the transom clearance Froude number operates in an off-design condition. The resistance reduction due to the TPD results in an unloading of the propeller and a better operating condition. Therefore, the total gain in the delivered power is achieved through the resistance reduction as well as a more favourable operating condition for the propeller.

Although the TPD position was optimized for Fn = 0.4, it is still effective both below and above this number. CFD results also reveal that the TPD can be more effective when the thrust is distributed to two propellers rather than one.

CRediT authorship contribution statement

Arash Eslamdoost: Conceptualization, Methodology, Validation, Formal analysis, Investigation, Writing – original draft, Writing – review & editing, Visualization, Project administration, Funding acquisition. **Lars Larsson:** Conceptualization, Methodology, Formal analysis, Writing – review & editing, Supervision, Project administration, Funding acquisition. **Matz Brown:** Conceptualization, Methodology, Formal analysis, Investigation, Writing – review & editing.

Declaration of competing interest

The authors declare that they have no known competing financial interests or personal relationships that could have appeared to influence the work reported in this paper.

Acknowledgement

The support from Kongsberg Maritime in Sweden through Chalmers University Technology Centre and The Swedish Transport Administration (Trafikverket) through the grant FUD 6482 (2018) is gratefully acknowledged. The simulations were performed on high-performance computing resources at Chalmers Centre for Computational Science and Engineering (C3SE) as well as the National Supercomputer Centre at Linköping University (NSC) provided by the Swedish National Infrastructure for Computing (SNIC). SSPA Sweden AB is acknowledged for providing the experimental data.

References

Bhushan, S., Xing, T., Stern, F., 2012. Vortical structures and instability analysis for Athena wetted transom flow with full-scale validation. J. Fluids Eng. Trans. ASME 134 (3), 031201. https://doi.org/10.1115/1.4006173.

Doctors, L.J., 2006. Influence of the transom-hollow length on wave resistance. In: International Workshop on Water Waves and Floating Bodies (IWWWFB). Loughborough, UK.

Doctors, L.J., Macfarlane, G.J., Young, R., 2007. A study of transom-stern ventilation. Int. Shipbuild. Prog. 54, 145–163.

Eça, L., Hoekstra, M., 2014. A procedure for the estimation of the numerical uncertainty of CFD calculations based on grid refinement studies. J. Comput. Phys. 262, 104–130. https://doi.org/10.1016/j.jcp.2014.01.006.

Eslamdoost, A., Larsson, L., Bensow, R., 2015. On transom clearance. Ocean. Eng. 99, 55–62. https://doi.org/10.1016/j.oceaneng.2015.02.008.

Eslamdoost, A., Larsson, L., Brown, M., 2020. A Device for Reducing the Resistance of Water Surface Vessels. SE542220 C2.

Haase, M., Binns, J.R., Thomas, G., Bose, N., 2016. Wave-piercing catamaran transom stern ventilation process. Ship Technol. Res. 63, 71–80. https://doi.org/10.1080/09377255.2015.1119922.

Hendrickson, K., Weymouth, G.D., Yu, X., Yue, D.K.-P., 2019. Wake behind a three-dimensional dry transom stern. Part 1. Flow structure and large-scale air entrainment. J. Fluid Mech. 875, 854–883. https://doi.org/10.1017/jfm.2019.505.

ITTC 28 Resistance Committee, 2017. Recommended Procedures and Guidelines: Ship Models.

Larsson, L., Raven, H.C., 2010. Ship Resistance and Flow, first ed. The Society of Naval Architects and Marine Engineers, Jersey City, New Jersey.

Maki, K.J., 2006. Transom Stern Hydrodynamics. Ph.D. thesis, Department of Naval Architecture and Marine Engineering, The University of Michigan.

Maki, K.J., Doctors, L.J., Beck, R.F., Troesch, A.W., 2006. Transom-stern flow for high-speed craft. Austrailian J. Mech. Eng. 3, 191–199. https://doi.org/10.1080/14484846.2006.11464508.

Merciar, J.A., Savitsky, D., 1973. Resistance of Transom Stern Craft in the Pre-planing Regime. Report number: SIT-DL-73-1667. Davidson Laboratory, Stevens Institute of Technology, Hoboken, New Jersey.

Oving, A.J., 1986. Resistance Prediction Method for Semi-planing Catamarans with Symmetrical Demi-Hulls. M.Sc. thesis. Department of Marine and Transport Technology, Delft University of Technology (Wageningen) M.Sc. thesis.

Starke, B., Raven, H., van der Ploeg, A., 2007. Computation of transom-stern flows using a steady free-surface fitting RANS method. In: 9th International Conference on Numerical Ship Hydrodynamics. Ann Arbor, Michigan, US.

van der Ploeg, A., Starke, B., 2013. Prediction of the transom flow regime with viscous free surface computations. Mar. 2011, IV Int. Conf. Comput. Methods Mar. Eng. 29, 261–272.

Wyatt, D.C., Fu, T.C., Taylor, G.L., Terrill, E.J., Xing, T., Bhushan, S., O'Shea, T.T., Dommermuth, D.G., 2008. A comparison of full-scale experimental measurements and computational predictions of the transom-stern wave of the R/V Athena I. In: 27th Symposium on Naval Hydrodynamics. Seoul, KOREA.